

Large non-reciprocal propagation of surface acoustic waves in epitaxial ferromagnetic/semiconductor hybrid structures

A. Hernández-Mínguez,^{1,*} F. Macià,² J. M. Hernández,² J. Herfort,¹ and P. V. Santos¹

*¹Paul-Drude-Institut für Festkörperelektronik,
Leibniz-Institut im Forschungsverbund Berlin e.V.,
Hausvogteiplatz 5-7, 10117 Berlin, Germany*

*²Dept. of Condensed Matter Physics, University of Barcelona,
Martí i Franquès 1, 08028 Barcelona, Spain*

(Dated: March 12, 2020)

Abstract

Non-reciprocal propagation of sound, that is, the different transmission of acoustic waves traveling along opposite directions, is a challenging requirement for the realization of devices like acoustic isolators and circulators. Here, we demonstrate the efficient non-reciprocal transmission of surface acoustic waves (SAWs) propagating along opposite directions of a GaAs substrate coated with an epitaxial Fe₃Si film. The non-reciprocity arises from the acoustic attenuation induced by the magneto-elastic (ME) interaction between the SAW strain field and spin waves in the ferromagnetic film, which depends on the SAW propagation direction and can be controlled via the amplitude and orientation of an external magnetic field. The acoustic transmission non-reciprocity, defined as the difference between the transmitted acoustic power for forward and backward propagation under ME resonance, reaches values of up to 20%, which are, to our knowledge, the largest non-reciprocity reported for SAWs traveling along a semiconducting piezoelectric substrate covered by a ferromagnetic film. The experimental results are well accounted for by a model for ME interaction, which also shows that non-reciprocity can be further enhanced by optimization of the sample design. These results make Fe₃Si/GaAs a promising platform for the realization of efficient non-reciprocal SAW devices.

I. INTRODUCTION

In the last years, there has been an increasing interest in the realization of non-reciprocal acoustic systems for the efficient manipulation of sound.¹ As acoustic propagation is reciprocal in linear systems preserving time reversibility,² it is possible to obtain non-reciprocal transmission by either introducing non-linear effects,^{3,4} or by breaking time-inversion symmetry. The last can be achieved by e.g. coupling the acoustic vibrations to a circulating fluid.⁵ Another option to induce local non-reciprocity is to take advantage of topologically protected acoustic modes propagating along the boundaries of periodic structures.⁶⁻⁹ These approaches have been mainly demonstrated for low-frequency sound waves ($\lesssim 1$ MHz) with wavelengths on the order of few millimeters, and the implementation of their working principles in miniaturized acoustic devices working at high frequencies ($\gtrsim 100$ MHz) might result very challenging.

Of special interest for applications are acoustic devices based on surface acoustic waves (SAWs). SAWs are elastic vibrations propagating along the surface of a solid with wavelengths reaching down to the sub- μm regime and frequencies up to several GHz. Due to their efficient piezoelectric generation and detection, and their low propagation velocities, SAWs have been successfully applied as radio-frequency filters and other kinds of signal processing in on-chip acousto-electric devices.¹⁰ In addition to this well-established technology, SAWs are ideally suited for controlling and interfacing elementary excitations in solid-state quantum systems like superconducting circuits,¹¹ defect centers¹²⁻¹⁵ and low-dimensional semiconductor structures.¹⁶⁻²² Therefore, the on-demand controlling of the acoustic propagation direction by means of non-reciprocal devices like SAW isolators and circulators would represent an important step towards the efficient acoustic interfacing between such quantum systems.

Non-reciprocal SAW propagation has been reported in systems like non-magnetic metals²³ and semiconductor heterostructures,²⁴ as well as in structures containing ferromagnetic materials.²⁵⁻²⁹ In the first case, non-reciprocity is caused by coupling the lattice strain to the cyclotron motion of free carriers under a strong magnetic field, while in the second case it is related to the non-symmetric transfer of momentum between the acoustic wave and electric currents applied parallel or anti-parallel to the SAW. In the last case, non-reciprocal propagation is induced by coupling the SAW strain field to the magnetization dynamics

of a ferromagnet through the magneto-elastic (ME) interaction. As the magnetization precesses only clockwise around its equilibrium direction, the propagation of circularly-polarized acoustic waves along the ferromagnet will depend on the helicity of the strain field relative to the magnetization direction.³⁰ The excitation of magnetoelastic waves was intensively studied in ferromagnetic insulators like yttrium iron garnet (YIG),^{31–35} where non-reciprocal SAW attenuation of up to two orders of magnitude was experimentally reported.^{25,26} However, YIG is a weak magnetoelastic material and, in addition, the non-piezoelectricity of YIG requires the incorporation of strong piezoelectric films like ZnO for the electric excitation of SAWs.^{25,26,36,37}

Another possibility to couple SAWs and magnetization is the deposition of a thin ferromagnetic film at the surface of a piezoelectric substrate. This approach has been demonstrated in LiNbO₃ covered by a poly-crystalline cobalt or nickel layer,^{27–29,38–44} and in ferromagnetic-semiconductor hybrid structures like GaMnAs/GaAs.^{45–47} Although non-reciprocal propagation has been demonstrated in the first case,^{27–29} the intrinsic structural disorder of poly-crystalline Ni leads to a magnetization response with a relatively large Gilbert damping coefficient $\alpha \sim 0.05$,⁴⁸ and therefore to wide ME resonances with weak non-reciprocal effects.^{27,29}

Here, we present an alternative hybrid structure for ME applications consisting of a Fe₃Si film grown epitaxially on a GaAs substrate. Fe₃Si is a binary Heusler-like ferromagnetic metal which has attracted interest as possible component in magneto-electronic devices.^{49,50} As its cubic crystal structure is almost lattice-matched to the GaAs substrate (mismatch $\leq 0.01\%$), it is possible to grow epitaxial films with high interfacial perfection and structural quality,^{51–53} thus leading to narrow ferromagnetic resonance (FMR) lines^{54,55} characterized by damping coefficients as low as $\alpha \approx 3 \times 10^{-4}$.⁵⁶ In addition, the shear magneto-elastic coefficient, b_2 , for thin films of this material has been estimated to be $b_2 \approx 2 - 7$ T.⁵⁵ This value is of the same order of magnitude as e.g. crystalline Fe and Ni,⁵⁷ thus making Fe₃Si a promising material for ME applications. Moreover, as SAW control and manipulation of quantum systems has mostly been demonstrated in GaAs-based semiconductor heterostructures,^{17–22} SAW isolators and circulators based on Fe₃Si/GaAs hybrids could provide an efficient integrated acoustic interface between such semiconductor-based quantum devices. Finally, in contrast to GaMnAs/GaAs, where the magnetic properties of GaMnAs require working at cryogenic temperatures,^{45–47,58,59} the high Curie temperature (above 800 K)⁶⁰ of Fe₃Si makes

this material suitable for room-temperature applications.

In this contribution, we demonstrate the non-reciprocal propagation of high-frequency SAWs (3.45 GHz) traveling on a Fe₃Si/GaAs hybrid structure. For well-defined orientations of the magnetization in the Fe₃Si film, the ME interaction transfers energy from the acoustic into the magnetic system, thus inducing SAW attenuation. The high structural quality of the film leads to very narrow ME-resonances lines (i.e., with full widths at half maximum as narrow as 2 mT). The strength of the ME-induced attenuation depends on the relative angle between magnetization orientation and SAW wave vector. The resulting acoustic transmission non-reciprocity, defined as the difference between the transmitted acoustic power for forward and backward SAW propagation under ME resonance, reaches values up to 20%. This non-reciprocal behavior is significantly larger than that reported for Ni/LiNbO₃ operating at similar frequencies, thus making Fe₃Si/GaAs hybrids a promising platform for the realization of non-reciprocal SAW devices like acoustic isolators and circulators in GaAs-based semiconductor heterostructures.

We have organized the manuscript as follows. Section II describes the fabrication process and the experimental procedure. In Section III, we characterize the magnetic and acoustic properties of our sample, and we present the experimental results on the non-reciprocal SAW propagation. In Section IV, we compare the results with the predictions of the theoretical model and give an outlook. Finally, Section V summarizes the main results of the manuscript.

II. EXPERIMENTAL DETAILS

The experiments were performed on a slightly non-stoichiometric Fe_{3+x}Si_{1-x} film with $x = 0.16$ (corresponding to a Si concentration of 21%) grown epitaxially on a GaAs(001) substrate by molecular beam epitaxy. Despite the non-stoichiometry, we will further refer to the material as Fe₃Si since the structural and magnetic properties of Fe_{3+x}Si_{1-x} epitaxial alloys are qualitatively very similar for $-0.07 \leq x \leq 0.6$.^{61,62} We fabricated the magneto-acoustic device sketched in Fig. 1 as follows. First, a clean c(4×4)-reconstructed GaAs surface was prepared by growing a 500-nm-thick GaAs buffer layer in a dedicated III-V semiconductor growth chamber using conventional growth parameters. The substrate was then transferred in ultra-high-vacuum into an As-free chamber, where the Fe₃Si film with a

thickness $d = 50$ nm was grown by co-deposition from high temperature effusion cells onto the GaAs at 200 °C.⁵¹ Next, we patterned the Fe₃Si film by optical lithography and wet chemical etching into octagonal mesas with a distance $L = 1.2$ mm between opposite sides. In the final fabrication step, we deposited pairs of interdigital transducers (IDTs) for the generation and detection of SAWs. The IDTs were patterned on the GaAs substrate at the opposite sides of the octagonal Fe₃Si mesa by electron beam lithography, metal evaporation and lift-off. Each IDT consists of 180 split-finger¹⁰ pairs with a 150 μm-wide aperture. The finger periodicity determines the SAW wavelength, which was set to $\lambda_{\text{SAW}} = 800$ nm.

Radio-frequency (RF) signals applied to the IDTs excite SAWs propagating with wave vector $k_{\text{SAW}} = 2\pi/\lambda_{\text{SAW}}$ parallel ($+k_{\text{SAW}}$) or anti-parallel ($-k_{\text{SAW}}$) to the $[110]$ direction of the Fe₃Si/GaAs hybrid structure. The acoustic delay line was characterized by measuring with a vector network analyzer the amplitude of the power transmission coefficient S_{21} of a SAW traveling from IDT₁ to IDT₂ ($+k_{\text{SAW}}$), as well as its S_{12} counterpart ($-k_{\text{SAW}}$). As the SAW is a Rayleigh mode, the strain tensor consists of three non-zero ε_{XX} , ε_{ZZ} and ε_{XZ} components,⁶³ expressed with respect to a rotated reference frame where the X -, Y -, and Z -axes point along the $[110]$, $[\bar{1}10]$ and $[001]$ crystallographic directions, respectively.

The ME experiments were performed by placing the magneto-acoustic device between the poles of an electromagnet for the application of a static in-plane magnetic field, \mathbf{H} . The sample was mounted on an electrically controlled rotation stage that settles the angle φ_H between \mathbf{H} and the $[110]$ surface direction of the Fe₃Si/GaAs hybrid structure (see Fig. 1). The angle φ_0 determines the equilibrium direction of the magnetization, $\mathbf{m} = \mathbf{M}/M_s$ (normalized to the saturation magnetization, M_s), defined as the direction that minimizes the magnetic free energy of the Fe₃Si film in absence of SAWs (see Supplemental Material). For each values of φ_H and the magnetic field strength, H , we measured both the forward (S_{21} , corresponding to a wave vector $+k_{\text{SAW}}$) and the backward (S_{12} , corresponding to $-k_{\text{SAW}}$) transmission coefficients of the SAW delay line. Then, we Fourier transformed the frequency-dependent measurements into the time domain to eliminate the electromagnetic cross-talk and analyze the amplitude of the SAW-related transmission peak. All measurements were performed at room temperature.

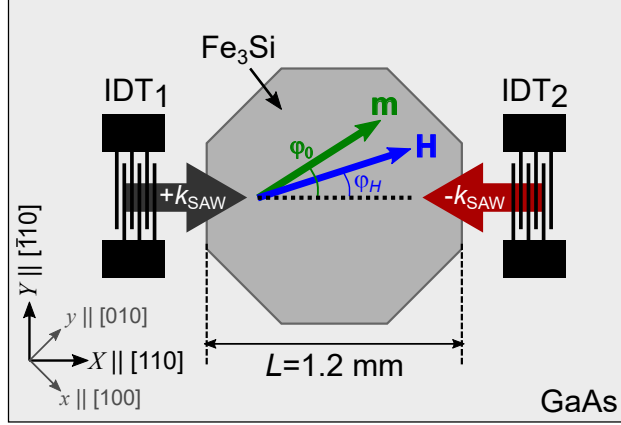


FIG. 1. Schematics of the magneto-acoustic device. Interdigital transducers (IDTs) at opposite ends of an Fe_3Si film launch and detect SAWs with wave vectors $\pm k_{\text{SAW}}$ along the $[110]$ crystallographic direction of the $\text{Fe}_3\text{Si}/\text{GaAs}$ hybrid structure. The angles φ_H and φ_0 determine the orientation of the external magnetic field, \mathbf{H} , and the equilibrium direction of the magnetization, \mathbf{m} , respectively, with respect to the $[110]$ surface direction.

III. RESULTS

The magnetic properties of the $\text{Fe}_3\text{Si}/\text{GaAs}$ hybrid structure were studied by FMR experiments. The color plot of Fig. 2(a) displays the dependence of the FMR signal on the static \mathbf{H} field applied along $[110]$ (horizontal axis) and on the frequency of an ac magnetic field (vertical axis) applied perpendicularly to \mathbf{H} . The low magnetic field branch ($\mu_0 H < 10$ mT) of the FMR curve represents the unsaturated state, where \mathbf{m} rotates towards \mathbf{H} as the magnetic field strength increases. The high magnetic field branch ($\mu_0 H > 10$ mT) corresponds to the saturated state, where \mathbf{m} and \mathbf{H} are fully aligned. This behavior indicates that the $[110]$ direction is one of the in-plane hard axes of the magnetization. The narrow FMR lines, with a width of less than 2 mT, attest to the good structural quality and low magnetic damping of the epitaxial material.⁵⁶ Figure 2(b) summarizes the dependence of the spin-wave frequency, f_{sw} , on the magnetic field strength when \mathbf{H} is applied along $[100]$ (black squares), $\bar{[110]}$ (red circles) and $[110]$ (blue triangles). The solid curves are fittings supposing spin waves with wave vector $\mathbf{q} = 0$, that is, the uniform precession mode measured in the FMR experiments (see Supplemental Material for a description of the theoretical model). The overlap of the $[110]$ and $\bar{[110]}$ curves confirms the negligible in-plane uniaxial anisotropy expected for the Fe concentration, growth conditions and film thickness of this sample.^{54,55,64} Therefore, the

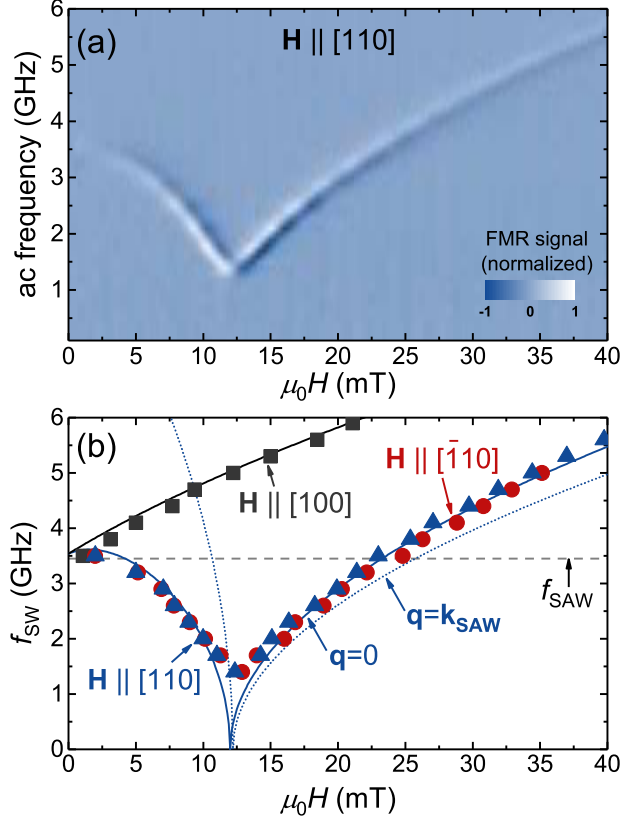


FIG. 2. (a) Dependence of the ferromagnetic resonance (FMR) signal of the Fe_3Si film on the strength of a static magnetic field \mathbf{H} applied along the $[110]$ direction (horizontal axis), and the frequency of the ac field (vertical axis) applied perpendicular to \mathbf{H} . (b) Spin-wave frequency, f_{SW} , as a function of the magnetic field strength when \mathbf{H} is applied along $[100]$ (black squares), $[\bar{1}10]$ (red circles) and $[110]$ (blue triangles). The solid curves are fittings supposing spin waves with wave vector $\mathbf{q} = 0$ (see Supplemental Material). The blue dotted curve is the calculated frequency of spin waves with $\mathbf{q} = \mathbf{k}_{\text{SAW}}$ and \mathbf{H} parallel to $[110]$. The horizontal dashed line indicates the SAW frequency (f_{SAW}) used in our magneto-acoustic device.

in-plane magnetization is only determined by the fourfold cubic crystalline anisotropy with easy axes pointing along $\langle 100 \rangle$ and hard axes along the $\langle 110 \rangle$ surface directions.

Figure 3(a) displays the dependence of S_{21} on the RF frequency applied to IDT_1 . The measurement was time-gated to remove the electromagnetic cross-talk between IDTs. The transmission spectrum shows a minimum insertion loss of 59 dB (maximum transmission) at the IDT resonant frequency $f_{\text{SAW}} = v_{\text{SAW}}/\lambda_{\text{SAW}} = 3.455$ GHz, where v_{SAW} is the SAW propagation velocity in GaAs. By Fourier transforming the frequency spectrum, we obtained

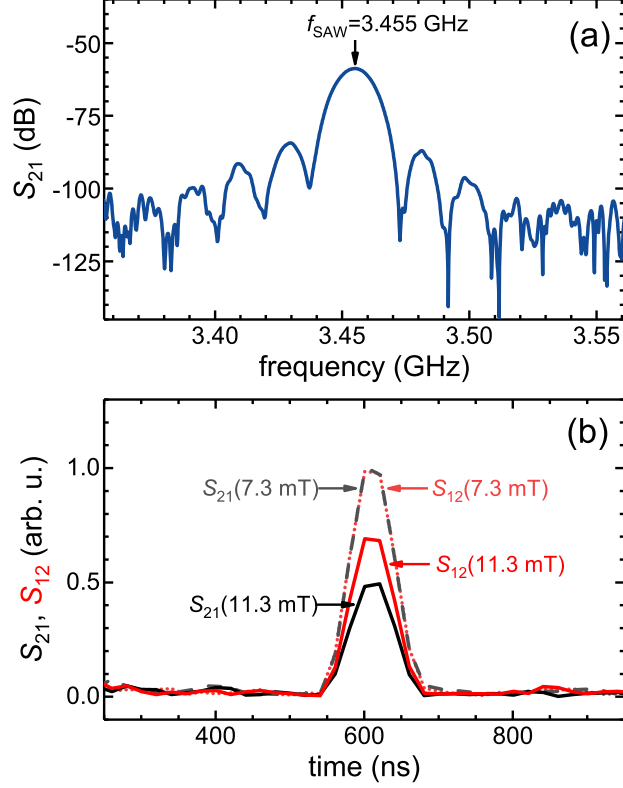


FIG. 3. (a) Dependence of S_{21} scattering parameter (corresponding to the RF power transmission coefficient) on the RF frequency applied to IDT₁. The spectrum was time-gated to remove the electromagnetic cross-talk. The minimum insertion loss (maximum transmission) occurs at the resonance frequency $f_{\text{SAW}} = 3.455$ GHz. (b) Time-resolved S_{21} and S_{12} coefficients measured for $\varphi_H = -0.6^\circ$ for two different magnetic field strengths. The peak delays at $\Delta t = 610$ ns correspond to the SAW propagation time between the IDTs. The curves are normalized to the magnitude of the S_{21} transmission peak for $\mu_0 H = 7.3$ mT.

the profile of S_{21} in the time domain shown in Fig. 3(b) (grey dashed curve). The peak at the time delay $\Delta t \approx 610$ ns is attributed to the arrival of the SAW after traveling from IDT₁ to IDT₂. The value of Δt corresponds closely to the acoustic propagation time $\Delta l/v_{\text{SAW}}$ over the center-to-center distance ($\Delta l = 1.75$ mm) between the IDTs. The same peak is observed for the time-resolved S_{12} coefficient, i.e. for SAW transmission from IDT₂ to IDT₁ (light red dotted curve).

If the external magnetic field brings the frequency and wave vector of spin waves in the Fe₃Si film into resonance with those of the SAW, then the ME interaction will excite spin waves in the ferromagnet for certain angles φ_0 between \mathbf{m} and the SAW wave vector.²⁸

Under these conditions, the ME coupling will convert acoustic into magnetic energy as the SAW propagates along the film, thus resulting in SAW attenuation.^{27–29,40–43,46} As indicated in Fig. 2(b), the frequency of spin waves with wave vector $\mathbf{q} = \mathbf{k}_{\text{SAW}}$ (blue dotted curve) matches the SAW frequency (grey dashed line) for two different strengths of \mathbf{H} applied along [110]. For \mathbf{H} applied along $[\bar{1}10]$, in contrast, the spin-wave frequency lies always above 10 GHz, and therefore no resonant ME coupling is possible for this magnetic configuration. In the calculations (see Supplemental Material), we have taken into account the wave-vector dependence of the dipolar-dipolar interaction,^{40,65} but we have neglected the wave-vector dependence of the exchange interaction. This is justified because the spin wave stiffness constant $D = 240 \text{ meV}\text{\AA}^2$ of Fe_3Si (cf. Ref. 66) leads to a frequency shift $\Delta f \propto Dk_{\text{SAW}}^2$ of only 36 MHz with respect to the uniform precession mode ($\mathbf{q} = 0$) measured in the FMR experiments.

The ME coupling was investigated by measuring S_{21} and S_{12} as a function of \mathbf{H} applied along the $[\bar{1}10]$ and [110] directions. As expected from our calculations, we did not observe SAW attenuation for \mathbf{H} parallel to $[\bar{1}10]$. In contrast, the SAW is clearly attenuated for well-defined values of \mathbf{H} applied along [110]. Figure 3(b) compares the time-resolved S_{21} and S_{12} coefficients for two magnetic field strengths applied at an angle $\varphi_H = -0.6^\circ$. Away of the ME resonance (for $\mu_0 H = 7.3 \text{ mT}$), the intensities of the S_{21} (gray dashed curve) and S_{12} (light red dotted curve) transmission peaks are exactly the same, thus confirming the reciprocal behavior of the SAW delay line. When the magnetic field increases to $\mu_0 H = 11.3 \text{ mT}$, the acoustic and magnetic systems enter into resonance leading to a decrease of both S_{21} and S_{12} peaks. Most important, the SAW transmission under ME resonance is clearly different for SAWs propagating with wave vectors $+k_{\text{SAW}}$ and $-k_{\text{SAW}}$. For S_{21} (solid black curve), the ME coupling reduces the transmitted SAW power to 50% of the corresponding out-of-resonance value, while for S_{12} (solid red curve) the transmission of the SAW peak is still 70% of the out-of-resonance one. The difference between these values yields a transmission non-reciprocity of 20% for SAWs traveling along opposite directions.

To get further insight into the non-reciprocal behavior, we have measured S_{21} and S_{12} for a range of H and φ_H values to determine the SAW attenuation $A = 1 - T$. Here, T represents the area of the SAW transmission peak in the time-domain spectrum, normalized to the corresponding area for H away from the ME resonance. Figure 4 shows the dependence of $A(\pm k_{\text{SAW}})$ on H measured at four angles φ_H . Each trace shows two ME resonances at

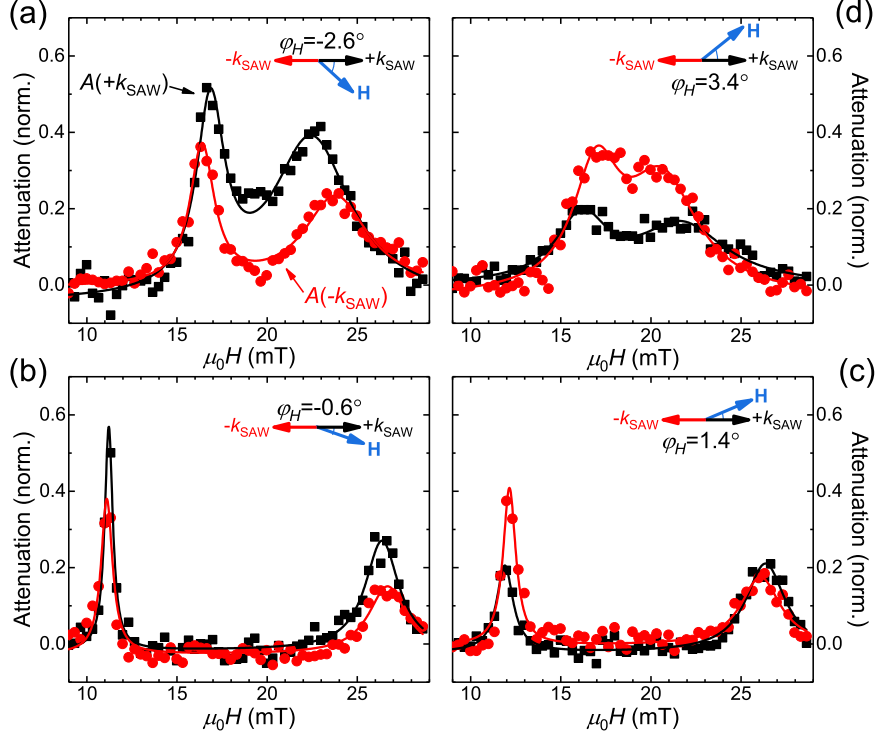


FIG. 4. Dependence of the ME-induced SAW attenuation, A , on the magnetic field amplitude, H , for SAWs with $+k_{\text{SAW}}$ (black squares) and $-k_{\text{SAW}}$ (red circles). The panels show measurements taken for magnetic field angles: (a) $\varphi_H = -2.6^\circ$, (b) $\varphi_H = -0.6^\circ$, (c) $\varphi_H = 1.4^\circ$, and (d) $\varphi_H = 3.4^\circ$. The solid curves are Lorentzian fits to the ME resonance lines.

two field values. For the resonance at the low magnetic field, \mathbf{m} is still rotating towards \mathbf{H} , while \mathbf{m} and \mathbf{H} are fully aligned for the resonance at high magnetic field. The magnetic field distance between the two resonant fields is maximum for $\varphi_H \approx 0$, and their position agrees well with the values predicted by the crossing between spin-wave and SAW frequencies in Fig. 2(b). As \mathbf{H} rotates away from the $[110]$ direction, the resonances move towards each other until they merge at $|\varphi_H| \approx 4^\circ$. For larger values of φ_H , the frequency of the spin waves lies above the SAW frequency, and no ME resonances can be excited. For all four orientations of φ_H in Fig. 4, $A(+k_{\text{SAW}})$ (black squares) is clearly different from $A(-k_{\text{SAW}})$ (red circles) at the ME resonance, reaching a non-reciprocal attenuation efficiency $\Delta A = A(+k_{\text{SAW}}) - A(-k_{\text{SAW}}) \approx \pm 20\%$. Moreover, the sign of ΔA depends on the sign of the magnetic field angle: for $\varphi_H < 0$, $\Delta A > 0$, cf. Figs. 4(a) and 4(b), while for $\varphi_H > 0$ the situation reverses and $\Delta A < 0$, cf. Figs. 4(c) and 4(d).

The two-dimensional color plots of Fig. 5(a) and 5(b) summarize the dependence of the

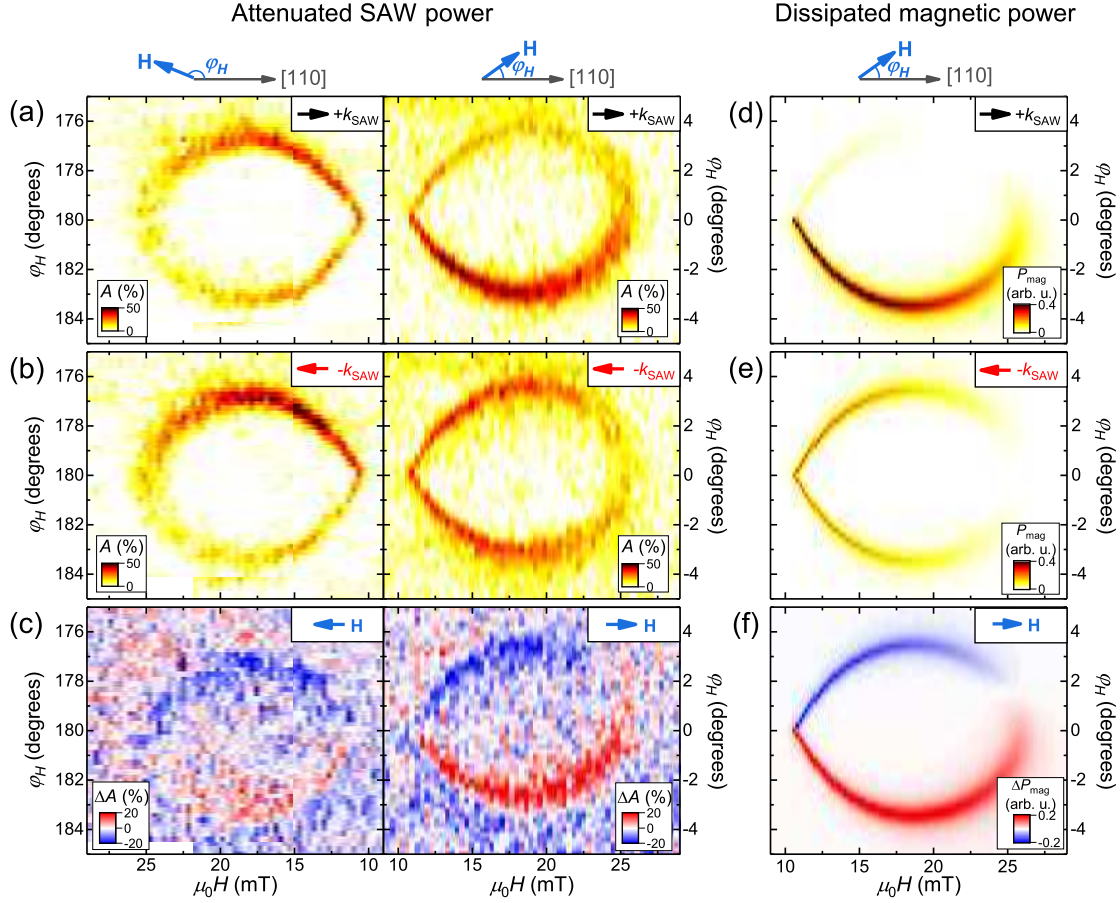


FIG. 5. ME-induced attenuation maps as a function of magnetic field strength, H , and angle, φ_H , for SAWs propagating with wave vectors (a) $+k_{\text{SAW}}$ and (b) $-k_{\text{SAW}}$. (c) SAW attenuation difference, ΔA , calculated from the data in panels (a) and (b). (d) Simulation of the magnetic power dissipated by the Fe_3Si film, P_{mag} , as a function of H and φ_H for SAW with wave vector $+k_{\text{SAW}}$. (e) Same as (d), but for SAW with wave vector $-k_{\text{SAW}}$. (f) Difference ΔP_{mag} between panels (d) and (e).

SAW attenuation on the strength H and angular direction φ_H (cf. sketch in the upper part of the figure) of the magnetic field. The resonant ME interaction (and, consequently, SAW attenuation) takes place only on a $\varphi_H \times H$ lobe defined by a very narrow range of angles φ_H around 0° and 180° . Figure 5(a) shows experimental data recorded for \mathbf{H} directions quasi-parallel (right panel, $-5^\circ < \varphi_H < 5^\circ$) and quasi-antiparallel (left panel, $175^\circ < \varphi_H < 185^\circ$) to $+k_{\text{SAW}}$. Figure 5(b) displays the corresponding data for SAW with wave vector $-k_{\text{SAW}}$. For all configurations, the attenuation changes as the magnetic field rotates away from the $[110]$ axis. For the quasi-parallel configurations (right panel of Fig. 5(a) and left panel of

Fig. 5(b)), the magnitude of the attenuation is strongly angular dependent with clearly different values in the upper and lower side of the $\varphi_H \times H$ lobes. In the quasi-antiparallel case, in contrast, the angular dependence is less pronounced. As it will be discussed in the next section, this weaker dependence arises from small deviations of the SAW wave vector from the [110] axis.

Finally, we show in Fig. 5(c) the non-reciprocal attenuation efficiency, ΔA , determined from the difference between the data in the corresponding panels of Fig. 5(a) and 5(b). Both panels of this figure show different signs of ΔA in the upper and lower sides of the $\varphi_H \times H$ lobes. As in Fig. 4, ΔA in Fig. 5(c) reaches values as large as $\pm 20\%$. Taking this value together with the length L of the ferromagnetic film, we estimate a non-reciprocal attenuation rate, $\eta \approx \Delta A/L \approx 16\%$ /mm. For comparison, we have also estimated η from the attenuation values reported in the Ni/LiNbO₃ hybrid structures working at 2.24 GHz SAW frequency,^{27,29} obtaining $\eta \sim 1.6 \pm 0.9\%$ /mm. The latter is one order of magnitude lower than the ones obtained in the Fe₃Si/GaAs structures reported here.

IV. DISCUSSION

To theoretically analyze the experimental results, we have taken into account that, according to energy conservation, the attenuated SAW power must equal the power dissipated by the spin waves.^{28,42} Therefore, as a first approximation to the problem, we have just estimated the response of the magnetization to the SAW-induced ME field, and compared the power dissipated by the spin waves to the SAW attenuation profiles of Fig. 5. The magnetization dynamics is described by the Landau-Lifshitz-Gilbert (LLG) equation:^{67,68}

$$\dot{\mathbf{m}} = -\gamma \mathbf{m} \times \mu_0 \mathbf{H}_{\text{eff}} + \alpha \mathbf{m} \times \dot{\mathbf{m}}, \quad (1)$$

where μ_0 is the vacuum permeability, γ is the gyromagnetic ratio, α is the Gilbert damping constant, and the dot denotes the time derivative. The temporal evolution of \mathbf{m} depends on the effective magnetic field $\mu_0 \mathbf{H}_{\text{eff}} = -\vec{\nabla}_{\mathbf{m}} F$. Here, F is the free magnetic energy normalized to the saturation magnetization. In addition to the Zeeman, shape and crystalline anisotropy energies (see Supplemental Material), it includes the magneto-elastic energy, F_{me} , that couples the oscillating strain of the SAW to the magnetization. In a material with cubic symmetry, the lowest order contributions to F_{me} can be expressed as:⁵⁷

$$\begin{aligned}
F_{me} = & b_1[\varepsilon_{xx}m_x^2 + \varepsilon_{yy}m_y^2 + \varepsilon_{zz}m_z^2] \\
& + 2b_2[\varepsilon_{xy}m_xm_y + \varepsilon_{xz}m_xm_z + \varepsilon_{yz}m_y m_z],
\end{aligned} \tag{2}$$

where b_1 and b_2 represent the longitudinal and shear ME coefficients, respectively, while ε_{ij} and m_i are the projections of the strain and magnetization components onto the $\hat{\mathbf{x}} \parallel [100]$, $\hat{\mathbf{y}} \parallel [010]$ and $\hat{\mathbf{z}} \parallel [001]$ directions of the cubic lattice. As mentioned above, it is convenient to rewrite Eq. 2 as a function of the three non-zero strain components ε_{XX} , ε_{ZZ} and ε_{XZ} of the SAW expressed in the rotated XYZ reference frame, see Fig. 1. We will also describe \mathbf{m} in spherical coordinates with azimuthal and polar angles, φ and θ , expressed with respect to $[110]$ and $[001]$, respectively. A detailed derivation of the equations is presented in the Supplemental Material. For small angular deviations $\delta\varphi$ and $\delta\theta$ of \mathbf{m} with respect to its equilibrium direction, the effective ME field driving the magnetization precession, $\mu_0\mathbf{h} = -\vec{\nabla}_{\mathbf{m}}F_{me}$, consists of the following in-plane and out-of-plane components perpendicular to \mathbf{m} , h_φ and h_θ , respectively:

$$\mu_0h_\varphi = 2b_2 \sin(\varphi_0) \cos(\varphi_0)\varepsilon_{XX}, \tag{3}$$

$$\mu_0h_\theta = 2b_2 \cos(\varphi_0)\varepsilon_{XZ}. \tag{4}$$

The in-plane component h_φ is proportional to the longitudinal strain of the SAW, ε_{XX} , while the out-of-plane component h_θ is proportional to the shear strain, ε_{XZ} . Both components depend on the in-plane equilibrium direction of \mathbf{m} through φ_0 (see Fig. 1). In the absence of an external magnetic field, \mathbf{m} points along one of the $\langle 100 \rangle$ easy axes (i.e., $\varphi_0 = \pm 45^\circ$). When \mathbf{H} is applied along the $[\bar{1}10]$ direction, \mathbf{m} rotates toward $\varphi_0 \approx 90^\circ$, so that both h_φ and h_θ vanish. This, together with the large spin wave frequencies expected for this magnetic configuration, explain the absence of ME coupling for this orientation of \mathbf{H} . In contrast, when \mathbf{H} points along $[110]$, \mathbf{m} rotates toward $\varphi_0 \approx 0$. Here, h_φ also tends to zero, but now h_θ approaches its maximum value, provided the SAW strain component ε_{XZ} is not zero. As ε_{XZ} vanishes at a free surface, h_θ is usually very small for thin ferromagnetic films and/or large SAW wavelengths, and can normally be neglected.^{45,69,70} For thicker films and/or shorter SAW wavelengths, however, ε_{XZ} becomes relevant, and the contribution of

h_θ to the magnetization dynamics must be taken into account. To visualize this behavior, we display in Fig. 6(a) the amplitude of ε_{XX} and ε_{XZ} as a function of sample depth calculated for a $\lambda_{\text{SAW}} = 800$ nm SAW. The calculations of the SAW strain were carried out using an elastic model that takes into account the elastic properties of Fe_3Si ⁷¹ and GaAs ⁷². While ε_{XX} decreases from its maximum value as it crosses the film, ε_{XZ} increases from zero and reaches a value $\varepsilon_{XZ} \approx 0.5\varepsilon_{XX}$ at the $\text{Fe}_3\text{Si}/\text{GaAs}$ interface (marked as a vertical dashed line in Fig. 6(a)).

The observed non-reciprocal SAW attenuation can therefore be understood as an interplay between the h_φ and h_θ components.^{28,29} Due to the $\pi/2$ time phase shift between ε_{XX} and ε_{XZ} ,⁶³ the ME driving field $\mathbf{h} = h_\varphi\hat{\varphi} + ih_\theta\hat{\theta}$ is, in general, elliptically polarized. Its helicity depends on the ratio $\varepsilon_{XZ}/\varepsilon_{XX}$ and changes signs when one reverses the SAW propagation direction. As the magnetization precession described by the LLG equation has also a well-defined helicity, the strength of the ME coupling will depend on the helicity of \mathbf{h} .⁷³ For example, for a SAW propagating with $+k_{\text{SAW}}$, $\varepsilon_{XX} \propto \cos\omega t$ and $\varepsilon_{XZ} \propto \sin\omega t$. If \mathbf{H} rotates the magnetization towards $0 < \varphi_0 < 45^\circ$, then \mathbf{h} and \mathbf{m} will precess with opposite helicities and the coupling of the SAW to the magnetization dynamics will be weak, see right panel in Fig. 5(a). However, if \mathbf{H} orients \mathbf{m} towards $-45^\circ < \varphi_0 < 0$, the sign of h_φ will reverse and now both \mathbf{h} and \mathbf{m} will precess with the same helicity. Under these conditions, the ME coupling will be strong, thus inducing a larger SAW attenuation. When \mathbf{H} reverses and the magnetization points against the SAW wave vector, h_θ changes sign and inverts the helicity dependence of \mathbf{h} on φ_0 . The same happens if the magnetization stays along $[110]$, but the SAW propagates with $-k_{\text{SAW}}$, causing $\varepsilon_{XZ} \propto \sin\omega t$ to be replaced by $\varepsilon_{XZ} \propto -\sin\omega t$. Finally, when both magnetization and SAW wave vector are reversed, h_θ remains positive and the original dependence on the relative angle between \mathbf{H} and SAW wave vector is recovered, see the left panel in Fig. 5(b).

According to the previous discussion, the SAW attenuation profiles for quasi-parallel and quasi-antiparallel configurations of \mathbf{H} and SAW wave vector in Fig. 5(a) and 5(b) should be mirror images of each other. However, as already mentioned in the previous section, this is not exactly the case for the experimental data. We attribute this discrepancy to a small, unintentional misalignment angle β between the SAW wave vector and the $[110]$ direction, probably caused during the patterning of the IDTs. This misalignment breaks the symmetry of h_φ and h_θ by introducing additional terms that depend on β and b_1 (see Supplemental

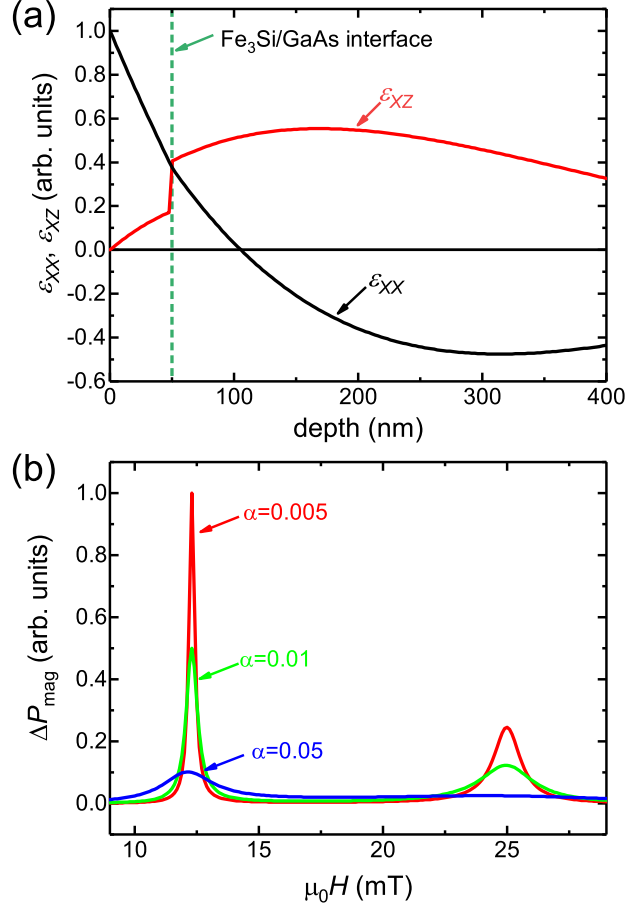


FIG. 6. (a) Dependence of the longitudinal and shear strain amplitudes, ε_{XX} (black curve) and ε_{XZ} (red curve), respectively, on sample depth for a SAW with 800 nm wavelength. The curves are normalized with respect to the amplitude of ε_{XX} at the top surface. The vertical dashed line indicates the position of the Fe₃Si/GaAs interface. (b) Difference in dissipated magnetic power, ΔP_{mag} , for the parallel and anti-parallel configurations of H and k_{SAW} , as a function of the Gilbert damping coefficient α . The data were calculated for $f_{\text{SAW}} = 3.45$ GHz, $\varphi_H = -1.5^\circ$, $\varepsilon_{XZ} = 0.5\varepsilon_{XX}$ and $\beta = 0$, and are normalized with respect to the maximum value for $\alpha = 0.005$.

Material). As a consequence, the non-reciprocity with respect to φ_0 is enhanced in the quasi-parallel configuration, but partially compensated in the quasi-antiparallel configuration. To confirm this assumption, we have estimated the dependence on H and φ_H of the power dissipated by the spin waves and compared it to the profiles in Fig. 5(a) and (b). The dissipated magnetic power, P_{mag} , can be calculated as:²⁸

$$P_{\text{mag}} = -\text{Im} \left[\mu_0 \frac{\omega}{2} \int_{V_0} (\mathbf{h}^* \bar{\chi} \mathbf{h}) dV \right], \quad (5)$$

where $\bar{\chi}$ is the Polder susceptibility tensor describing the response of the magnetization to \mathbf{h} , and V_0 is the volume of the ferromagnetic film traversed by the SAW. To obtain $\bar{\chi}$, we have solved the linearized LLG equation supposing harmonic solutions for ε_{XX} , ε_{XZ} , $\delta\theta$ and $\delta\varphi$. A detailed derivation is presented in the Supplemental Material. Although an accurate calculation of P_{mag} requires the integration of $\mathbf{h}^* \bar{\chi} \mathbf{h}$ taking into account the variation of ε_{XX} and ε_{XZ} across the depth of the Fe₃Si film, we have just estimated $\mathbf{h}^* \bar{\chi} \mathbf{h}$ close to the Fe₃Si/GaAs interface. This depth yields the largest $\varepsilon_{XZ}/\varepsilon_{XX}$ ratio, see Fig. 6(a), where one expects the strongest non-reciprocal effect. In the simulation, we have used the values of the gyromagnetic ratio, shape and cubic anisotropies obtained from the fitting of the FMR curves in Fig. 2. The width of the ME resonance depends on the damping coefficient, which was set to $\alpha = 8 \times 10^{-3}$. The degree of non-reciprocity depends on the values of b_1 , b_2 , ε_{XX} , ε_{XZ} and β , which we have set to $b_1 = 6$ T, $b_2 = 2$ T, $\varepsilon_{XX} = 10^{-4}$, $\varepsilon_{XZ} = 0.5 \times 10^{-4}$ and $\beta = 1^\circ$. Figures 5(d) and 5(e) display P_{mag} for \mathbf{H} and SAW wave vector in the quasi-parallel and quasi-antiparallel configurations, respectively, while the difference ΔP_{mag} between both configurations is shown in Fig. 5(f). The theoretical model reflects qualitatively well the position of the ME resonances, their amplitude dependence on H and φ_H and the non-reciprocal behavior.

To conclude this section, we briefly discuss the reasons for the superior non-reciprocal SAW propagation of the Fe₃Si/GaAs hybrid structure compared to the poly-crystalline nickel on LiNbO₃. The first is the high degree of structural quality of our epitaxial Fe₃Si film, which ensures the low Gilbert damping coefficient required for the observation of the strong non-reciprocal effects. To illustrate this point, we have estimated ΔP_{mag} as a function of H for a fixed value of φ_H and several values of α . The results are displayed in Fig. 6(b), normalized with respect to the maximum value for $\alpha = 0.005$. We observe that ΔP_{mag} is inversely proportional to α , and becomes ten times smaller when α increases from 0.005 to 0.05. This is in good agreement with the difference in the calculated values of η for the Fe₃Si/GaAs and Ni/LiNbO₃ systems.

The second reason is the short SAW wavelength used in our experiment (800 nm), which is about two times smaller than in the Ni/LiNbO₃ (1.5 μm) structures. This implies a larger $\varepsilon_{XZ}/\varepsilon_{XX}$ ratio at the ferromagnetic film and, therefore, a larger degree of elliptical

polarization of the effective ME field driving the magnetization precession. Following this approach, it should be possible to further improve the sample design to get SAW isolators with non-reciprocal transmission exceeding 10 dB. This will happen when the SAW-induced ME field is fully circularly polarized, that is, when $|h_\varphi| = |h_\theta|$. According to Eqs. 3 and 4, this condition fulfills when $\varepsilon_{XZ}/\varepsilon_{XX} = \sin(\varphi_0)$. For instance, when $\varepsilon_{XZ}/\varepsilon_{XX} = 0.5$, the maximum non-reciprocity will happen if ME resonance takes place for $\varphi_0 = 30^\circ$. It should be possible to get close to these conditions by an accurate selection of Fe₃Si film thickness and SAW frequency.

Finally, an alternative approach to increase the degree of non-reciprocity has recently been proposed.^{74,75} It consists in modifying the spin-wave frequency dispersion curves, so that the frequency crossing points for SAWs and spin waves propagating along $-k_{\text{SAW}}$ differ from the ones expected in the $+k_{\text{SAW}}$ case. This can be done e.g. by covering the Fe₃Si film with a heavy metal capping layer,⁷⁴ or by fabricating structures consisting of two ferromagnetic films close to each other with opposite magnetization directions.⁷⁵ As epitaxial trilayers consisting of two Fe₃Si films separated either by a thin metal⁷⁶ or semiconductor spacer^{77,78} have already been reported, Fe₃Si/GaAs hybrid structures could be a promising system for the experimental implementation of this mechanism.

V. CONCLUSIONS

In this contribution, we have demonstrated non-reciprocal propagation of SAWs along a GaAs substrate covered with an epitaxial Fe₃Si film. For well-defined values of the external magnetic field, the magneto-elastic coupling transfers energy from the acoustic into the magnetic system, thus inducing attenuation of the SAW. The strength of the SAW attenuation depends on the relative orientation between magnetization and SAW wave vector, and leads to attenuation differences of up to 20% for SAWs propagating along opposite directions. We attribute the non-reciprocal behavior to the dependence of the magnetization dynamics on the helicity of the elliptically polarized magneto-elastic field associated to the SAW. Our simulations confirm these results and show that non-zero longitudinal and shear strain at the ferromagnetic film, as well as low magnetic damping, are critical to achieve large non-reciprocal effects. Due to the combination of large magnetostriction, low magnetic damping, and the possibility of growing multilayers, epitaxial Fe₃Si/GaAs hybrids

are promising systems for the realization of non-reciprocal acoustic devices in GaAs-based semiconductor heterostructures.

ACKNOWLEDGEMENTS

The authors would like to thank Manfred Ramsteiner for a critical reading of the manuscript, as well as H.-P. Schönherr, S. Rauwerdink and S. Meister for technical support in the preparation of the samples.

* alberto.h.minguez@pdi-berlin.de

- ¹ R. Fleury, D. Sounas, M. R. Haberman, and A. Al, *Acoustics Today* **11**, 14 (2015).
- ² A. Maznev, A. Every, and O. Wright, *Wave Motion* **50**, 776 (2013).
- ³ B. Liang, X. S. Guo, J. Tu, D. Zhang, and J. C. Cheng, *Nat. Mater.* **9**, 989 (2010).
- ⁴ B.-I. Popa and S. A. Cummer, *Nat. Comm.* **5**, 3398 (2014).
- ⁵ R. Fleury, D. L. Sounas, C. F. Sieck, M. R. Haberman, and A. Alù, *Science* **343**, 516 (2014).
- ⁶ A. B. Khanikaev, R. Fleury, S. H. Mousavi, and A. Alù, *Nat. Comm.* **6**, 8260 (2015).
- ⁷ S. D. Huber, *Nat. Phys.* **12**, 621 (2016).
- ⁸ H. Chen, H. Nassar, A. N. Norris, G. K. Hu, and G. L. Huang, *Phys. Rev. B* **98**, 094302 (2018).
- ⁹ R. Fleury, M. R. Haberman, G. Huang, and A. N. Norris, *J. Acoust. Soc. Am.* **146**, 719 (2019).
- ¹⁰ C. K. Campbell, *Surface Acoustic Wave Devices for Mobile and Wireless Communications*, edited by R. Stern and M. Levy (Academic Press, Inc., 1998).
- ¹¹ M. V. Gustafsson, T. Aref, A. F. Kockum, M. Ekström, G. Johansson, and P. Delsing, *Science* **346**, 207 (2014).
- ¹² D. A. Golter, T. Oo, M. Amezcua, K. A. Stewart, and H. Wang, *Phys. Rev. Lett.* **116**, 143602 (2016).
- ¹³ S. J. Whiteley, G. Wolfowicz, C. P. Anderson, A. Bourassa, H. Ma, M. Ye, G. Koolstra, K. Satzinger, M. V. Holt, F. J. Heremans, A. N. Cleland, D. I. Schuster, G. Galli, and D. D. Awschalom, *Nat. Phys.* **15**, 490 (2019).
- ¹⁴ S. Lazić, A. Espinha, S. P. Yanguas, C. Gibaja, F. Zamora, P. Ares, M. Chhowalla, W. S. Paz, J. J. Palacios Burgos, A. Hernández-Mínguez, P. V. Santos, and H. P. van der Meulen, *Comm.*

- Phys. **2**, 113 (2019).
- ¹⁵ F. Iikawa, A. Hernández-Mínguez, I. Aharonovich, S. Nakhaie, Y.-T. Liou, J. M. J. Lopes, and P. V. Santos, *Appl. Phys. Lett.* **114**, 171104 (2019).
- ¹⁶ C. Wiele, F. Haake, C. Rocke, and A. Wixforth, *Phys. Rev. A* **58**, R2680 (1998).
- ¹⁷ O. D. D. Couto, S. Lazić, F. Iikawa, J. A. H. Stotz, U. Jahn, R. Hey, and P. Santos, *Nat. Phot.* **3**, 645 (2009).
- ¹⁸ J. R. Gell, M. B. Ward, R. J. Young, R. M. Stevenson, P. Atkinson, D. Anderson, G. A. C. Jones, D. A. Ritchie, and A. J. Shields, *Appl. Phys. Lett.* **93**, 081115 (2008).
- ¹⁹ E. A. Cerda-Méndez, D. N. Krizhanovskii, M. Wouters, R. Bradley, K. Biermann, K. Guda, R. Hey, P. V. Santos, D. Sarkar, and M. S. Skolnick, *Phys. Rev. Lett.* **105**, 116402 (2010).
- ²⁰ R. P. G. McNeil, M. Kataoka, C. J. B. Ford, C. H. W. Barnes, D. Anderson, G. A. C. Jones, I. Farrer, and D. A. Ritchie, *Nature* **477**, 439 (2011).
- ²¹ S. Hermelin, S. Takada, M. Yamamoto, S. Tarucha, A. D. Wieck, L. Saminadayar, C. Bauerle, and T. Meunier, *Nature* **477**, 435 (2011).
- ²² S. Lazić, A. Violante, K. Cohen, R. Hey, R. Rapaport, and P. V. Santos, *Phys. Rev. B* **89**, 085313 (2014).
- ²³ J. Heil, B. Lüthi, and P. Thalmeier, *Phys. Rev. B* **25**, 6515 (1982).
- ²⁴ H. Zhu and M. Rais-Zadeh, *IEEE Electr. Dev. Lett.* **38**, 802 (2017).
- ²⁵ M. F. Lewis and E. Patterson, *Appl. Phys. Lett.* **20**, 276 (1972).
- ²⁶ M. R. Daniel, *J. Appl. Phys.* **48**, 1732 (1977).
- ²⁷ M. Weiler, L. Dreher, C. Heeg, H. Huebl, R. Gross, M. S. Brandt, and S. T. B. Goennenwein, *Phys. Rev. Lett.* **106**, 117601 (2011).
- ²⁸ L. Dreher, M. Weiler, M. Pernpeintner, H. Huebl, R. Gross, M. S. Brandt, and S. T. B. Goennenwein, *Phys. Rev. B* **86**, 134415 (2012).
- ²⁹ R. Sasaki, Y. Nii, Y. Iguchi, and Y. Onose, *Phys. Rev. B* **95**, 020407(R) (2017).
- ³⁰ C. Kittel, *Phys. Rev.* **110**, 836 (1958).
- ³¹ H. Matthews and H. van de Vaart, *Appl. Phys. Lett.* **15**, 373 (1969).
- ³² M. Tsutsumi, T. Bhattacharyya, and N. Kumagai, *J. Appl. Phys.* **46**, 5072 (1975).
- ³³ P. R. Emtage, *Phys. Rev. B* **13**, 3063 (1976).
- ³⁴ G. Komoriya and G. Thomas, *J. Appl. Phys.* **50**, 6459 (1979).
- ³⁵ R. E. Camley, *J. Appl. Phys.* **50**, 5272 (1979).

- ³⁶ Y. Shimizu, K. Hasegawa, and T. Yamada, *Electron. Commun. Jpn., Part I* **63**, 1 (1980).
- ³⁷ N. I. Polzikova, S. G. Alekseev, I. I. Pyataikin, I. M. Kotelyanskii, V. A. Luzanov, and A. P. Orlov, *AIP Advances* **6**, 056306 (2016).
- ³⁸ A. K. Ganguly, K. L. Davis, D. C. Webb, and C. Vittoria, *J. Appl. Phys.* **47**, 2696 (1976).
- ³⁹ S. Davis, A. Baruth, and S. Adenwalla, *App. Phys. Lett.* **97**, 232507 (2010).
- ⁴⁰ P. G. Gowtham, T. Moriyama, D. C. Ralph, and R. A. Buhrman, *J. Appl. Phys.* **118**, 233910 (2015).
- ⁴¹ D. Labanowski, A. Jung, and S. Salahuddin, *Appl. Phys. Lett.* **108**, 022905 (2016).
- ⁴² P. G. Gowtham, D. Labanowski, and S. Salahuddin, *Phys. Rev. B* **94**, 014436 (2016).
- ⁴³ X. Li, D. Labanowski, S. Salahuddin, and C. S. Lynch, *J. Appl. Phys.* **122**, 043904 (2017).
- ⁴⁴ R. Sasaki, Y. Nii, and Y. Onose, *Phys. Rev. B* **99**, 014418 (2019).
- ⁴⁵ L. Thevenard, J.-Y. Duquesne, E. Peronne, H. J. von Bardeleben, H. Jaffres, S. Ruttala, J.-M. George, A. Lemaître, and C. Gourdon, *Phys. Rev. B* **87**, 144402 (2013).
- ⁴⁶ L. Thevenard, C. Gourdon, J. Y. Prieur, H. J. von Bardeleben, S. Vincent, L. Becerra, L. Largeau, and J.-Y. Duquesne, *Phys. Rev. B* **90**, 094401 (2014).
- ⁴⁷ L. Thevenard, I. S. Camara, S. Majrab, M. Bernard, P. Rovillain, A. Lemaître, C. Gourdon, and J.-Y. Duquesne, *Phys. Rev. B* **93**, 134430 (2016).
- ⁴⁸ J. Walowski, M. D. Kaufmann, B. Lenk, C. Hamann, J. McCord, and M. Mnzenberg, *J. Phys. D: Appl. Phys.* **41**, 164016 (2008).
- ⁴⁹ J. Herfort, H.-P. Schönherr, A. Kawaharazuka, M. Ramsteiner, and K. Ploog, *J. Cryst. Growth* **278**, 666 (2005).
- ⁵⁰ A. Ionescu, C. A. F. Vaz, T. Trypiniotis, C. M. Gürtler, H. García-Miquel, J. A. C. Bland, M. E. Vickers, R. M. Dalgliesh, S. Langridge, Y. Bugoslavsky, Y. Miyoshi, L. F. Cohen, and K. R. A. Ziebeck, *Phys. Rev. B* **71**, 094401 (2005).
- ⁵¹ J. Herfort, H.-P. Schönherr, and K. H. Ploog, *Appl. Phys. Lett.* **83**, 3912 (2003).
- ⁵² J. Thomas, J. Schumann, H. Vinzelberg, E. Arushanov, R. Engelhard, O. G. Schmidt, and T. Gemming, *Nanotechnology* **20**, 235604 (2009).
- ⁵³ C. Gusenbauer, T. Ashraf, J. Stangl, G. Hesser, T. Plach, A. Meingast, G. Kothleitner, and R. Koch, *Phys. Rev. B* **83**, 035319 (2011).
- ⁵⁴ K. Lenz, E. Kosubek, K. Baberschke, H. Wende, J. Herfort, H.-P. Schönherr, and K. H. Ploog, *Phys. Rev. B* **72**, 144411 (2005).

- ⁵⁵ M. Wegscheider, G. Käferböck, C. Gusenbauer, T. Ashraf, R. Koch, and W. Jantsch, *Phys. Rev. B* **84**, 054461 (2011).
- ⁵⁶ K. Lenz, E. Kosubek, K. Baberschke, J. Herfort, H.-P. Schönherr, and K. H. Ploog, *phys. stat. sol. (c)* **3**, 122 (2006).
- ⁵⁷ R. C. O’Handley, “Modern magnetic materials, principles and applications,” (John Wiler & Sons, Inc., 2000) Chap. 7, p. 230.
- ⁵⁸ A. V. Scherbakov, A. S. Salasyuk, A. V. Akimov, X. Liu, M. Bombeck, C. Brüggemann, D. R. Yakovlev, V. F. Sapega, J. K. Furdyna, and M. Bayer, *Phys. Rev. Lett.* **105**, 117204 (2010).
- ⁵⁹ M. Bombeck, A. S. Salasyuk, B. A. Glavin, A. V. Scherbakov, C. Brüggemann, D. R. Yakovlev, V. F. Sapega, X. Liu, J. K. Furdyna, A. V. Akimov, and M. Bayer, *Phys. Rev. B* **85**, 195324 (2012).
- ⁶⁰ Y. Nakamura, “Landolt-börnstein, new series iii/19c,” (Springer, Berlin, 1988) p. 26.
- ⁶¹ O. Kubaschewski, *Iron-Binary Phase Diagrams* (Springer, Berlin, 1982).
- ⁶² J. Herfort, H.-P. Schönherr, K.-J. Friedland, and K. H. Ploog, *J. Vac. Sci. Technol. B* **22**, 2073 (2004).
- ⁶³ L. Rayleigh, *Proc. London Math. Soc.* **s1-17**, 4 (1885).
- ⁶⁴ J. Herfort, H.-P. Schönherr, and B. Jenichen, *J. Appl. Phys.* **103**, 07B506 (2008).
- ⁶⁵ R. L. Stamps and B. Hillebrands, *Phys. Rev. B* **44**, 12417 (1991).
- ⁶⁶ M. Szymanski, M. Jankowski, L. Dobrzynski, A. Wisniewski, and S. Bednarski, *J. Phys. Condens. Matter* **3**, 4005 (1991).
- ⁶⁷ T. G. Gilbert, *Phys. Rev.* **100**, 1243 (1955).
- ⁶⁸ T. G. Gilbert, *IEEE Transactions on Magnetics* **40**, 3443 (2004).
- ⁶⁹ P. Kuszewski, I. S. Camara, N. Biarrotte, L. Becerra, J. von Bardeleben, W. S. Torres, A. Lemaître, C. Gourdon, J.-Y. Duquesne, and L. Thevenard, *J. Phys. Condens. Matter* **30**, 244003 (2018).
- ⁷⁰ P. Kuszewski, J.-Y. Duquesne, L. Becerra, A. Lemaître, S. Vincent, S. Majrab, F. Margailan, C. Gourdon, and L. Thevenard, *Phys. Rev. Appl.* **10**, 034036 (2018).
- ⁷¹ G. Kötter, K. Nembach, F. Wallow, and E. Nembach, *Mater. Sci. Eng., A* **114**, 29 (1989).
- ⁷² B. A. Auld, *Acoustic Fields and Waves in Solids* (Robert E. Krieger Publishing Company, Inc, Malabar, Florida, 1990).
- ⁷³ D. A. Stancil and A. Prabhakar, *Spin Waves, Theory and Applications* (Springer, 2009).

- ⁷⁴ R. Verba, I. Lisenkov, I. Krivorotov, V. Tiberkevich, and A. Slavin, Phys. Rev. Appl. **9**, 064014 (2018).
- ⁷⁵ R. Verba, V. Tiberkevich, and A. Slavin, Phys. Rev. Appl. **12**, 054061 (2019).
- ⁷⁶ B. Jenichen, U. Jahn, A. Nikulin, J. Herfort, and H. Kirmse, Semicond. Sci. Technol. **30**, 114005 (2015).
- ⁷⁷ S. Gaucher, B. Jenichen, J. Kalt, U. Jahn, A. Trampert, and J. Herfort, Appl. Phys. Lett. **110**, 102103 (2017).
- ⁷⁸ S. Gaucher, B. Jenichen, and J. Herfort, Semicond. Sci. Technol. **33**, 104005 (2018).